

<https://doi.org/10.1038/s43247-026-03242-3>

Atmospheric rivers and winter sea ice drive recent reversal in Antarctic ice mass loss

Check for updates

Marlen Kolbe ¹✉, Jose Abraham Torres Alavez², Ruth Mottram ², Marwan Katurji ³, Richard Bintanja^{4,5} & Eveline C. van der Linden ⁵

Since about 2000, the total mass of the Antarctic Ice Sheet has declined at a near-linear rate, increasing global sea levels. Since 2016, however, satellite gravimetry data reveal a slowdown in net Antarctic ice mass loss and a net mass gain since 2020, despite increases in dynamically-driven ice loss by discharge from outlet glaciers. Here we use a reanalysis and regional climate model to show that this reversal is primarily due to positive surface mass balance anomalies, which result from increased precipitation driven by enhanced atmospheric river activity, strengthened westerlies, and reduced sea ice extent. Atmospheric rivers have become more frequent and intense since 2020, particularly over the Antarctic Peninsula, Queen Maud Land, and Wilkes Land, resulting in strong regional positive mass balance anomalies. High-resolution regional climate model simulations with modified sea ice extent show that the effect of sea ice loss on enhancing precipitation through increased evaporation accounts for around 10% of the winter increase, but is overall minor compared to remote large-scale processes. Combined, these factors result in accumulation increases that currently offset the mass loss from accelerated ice discharge in Antarctica and point to processes important for future projections.

Antarctica holds the largest reservoir of freshwater on Earth; therefore, understanding the drivers of mass gains and losses of the Antarctic Ice Sheet (AIS) is crucial for predicting future global and regional sea level rise and associated changes in ocean circulation. Understanding the drivers of mass gains and losses for the AIS is crucial for predicting future sea level rise and changes in ocean circulation. Antarctica holds the largest reservoir of freshwater on Earth, and therefore changes in its ice mass balance strongly influence global and regional sea levels. Related freshwater influx and changes in the sea ice extent (SIE) can further affect density-driven global ocean circulation^{1–4}. AIS mass balance has shown a near-linear decline since 2002, but recent studies based on gravimetry-based estimates from the Gravity Recovery and Climate Experiment (GRACE) satellite missions and its successor GRACE-Follow-On (GRACE-FO) reveal an abrupt slowdown in mass loss between 2020 and 2022^{5,6}. This interruption in the downward trend has been attributed to anomalously high snowfall and resulting positive surface mass balance (SMB) anomalies, which were unprecedented in both West and East Antarctica^{5,7}. Updated GRACE data through

December 2024 show that ice mass accumulation has accelerated further due to even greater precipitation since 2022. A new ice discharge dataset⁸ confirms that this trend is not due to reduced ice discharge (which continues to accelerate), but is instead driven by enhanced surface accumulation, which more than compensates for the enhanced ice loss in the total mass budget.

Most precipitation on the AIS falls during short and intense episodic events, often in the form of atmospheric rivers (ARs)^{9–12}. In this study, we show that their intensity and persistence have increased since 2020, particularly in areas where mass balance anomalies identified by the GRACE satellite data are highest, namely the Antarctic Peninsula (AP), Queen Maud Land and Wilkes Land. We examine the role of hemispheric and regional-scale climate indices ENSO (El Niño Southern Oscillation) and the related Southern Annular Mode (SAM) in driving regional-scale patterns. Additionally, we analyse the role of the low SIE in recent years by conducting pan-Antarctic experiments at 11 km resolution in a regional climate model (RCM) optimised for Antarctica with modified SIE for 1 year (July

¹Department of Earth, Ocean and Atmospheric Sciences, University of British Columbia, Vancouver, BC, Canada. ²National Centre for Climate Research, Danish Meteorological Institute, Copenhagen, Denmark. ³Faculty of Science, University of Canterbury, Christchurch, New Zealand. ⁴Faculty of Science and Engineering, Energy and Sustainability Research Institute Groningen, University of Groningen, Groningen, the Netherlands. ⁵Research and Development of Weather and Climate models, Royal Dutch Meteorological Institute, De Bilt, the Netherlands. ✉e-mail: mkolbe@eoas.ubc.ca

2021–June 2022), which includes four AR events, including the heatwave events of February 2022 on the AP^{13,14} and of March 2022 on the East Antarctic Ice Sheet (EAIS)^{15–18}.

Kittel et al.¹⁹ have assessed Antarctic SMB responses to sea ice concentration (SIC) and sea surface temperature (SST) by performing multi-decadal sensitivity experiments with a hydrostatic RCM with a 50 km resolution. The authors applied perturbations to SIC and SST, both separately and in combination, using ERA-Interim data. SIC was perturbed based on the minimum or maximum of the 3- and 6-cell neighbourhood, and SST was perturbed by 2 °C and 4 °C for ice-free grid cells. The total SMB changes (including ice shelves) due to sea ice perturbations alone ranged from –6.6% (for higher SIC) to +3.5% (for lower SIC), increasing to +12.7% when combined with a +4 °C SST perturbation. They also ran experiments prescribing SIC and SST fields from CMIP5 models, which resulted in similar magnitudes of SMB change.

In this study, we use a non-hydrostatic, high-resolution (11 km) RCM driven by ERA5 to explore two extreme sea ice states outside present-day variability: a completely ice-free Southern Ocean (noICE) and a high SIE scenario with 100% sea ice extending 5° equatorward of the present-day ice edge (exICE). These experiments are conducted over a single year (July 2021–June 2022), which includes four precipitation-heavy AR events. By examining how these events respond to large sea ice changes, we isolate the influence of SIE on AR-driven precipitation and Antarctic SMB. Our study demonstrates a link between the recent increase in Antarctic surface accumulation through 2024 and intensified AR frequency. To avoid introducing an additional thermodynamic signal, SSTs are not modified.

Results and discussion

Recent increase in Antarctic ice mass

From the beginning of this century until 2020, Antarctic mass loss was estimated to range between –90 and –142 Gt yr⁻¹^{15,6,20–22}. After the launch of GRACE-FO in 2018, Zhang et al.⁶ reported a reduction in mass loss to only –24.8 ± 52.1 Gt yr⁻¹ until 2022⁶, and Wang et al.⁵ reported a mass gain of 129.7 ± 69.6 Gt yr⁻¹ from 2021 to 2022⁵. Using gravitational mass balance (GMB) data to December 2024, we show that the recent years of mass gain were not short-term anomalies, but the beginning of a significant 5-year mass gain trend of 67.53 ± 31.4 Gt yr⁻¹ from 2020 to 2024 (Fig. 1a). This positive trend occurs despite higher rates of dynamic ice loss, with the AIS losing nearly 100 Gt yr⁻¹ more ice through grounding line discharge between 2020 and 2024 compared to 2003–2019 (Fig. 1e, h). Instead, the recent mass gain is driven by an increase in SMB, which is the sum of precipitation, evaporation and sublimation, and surface runoff. For ERA5 and the RCM HCLIM43, we approximate SMB as the sum of precipitation and net evaporation-sublimation. Over Antarctica, this approximation compares well with observations and the more advanced SMB calculations of the RCM RACMO²³ (we use RACMO2.4p; see ‘Methods’).

SMB remained near equilibrium until 2020 but has since then been rising at rates of ~200 Gt yr⁻¹ (219.9 ± 14.9 Gt yr⁻¹ in ERA5; 197.42 ± 17.7 Gt yr⁻¹ in RACMO2.4p; and 196.37 ± 13.6 Gt yr⁻¹ in HCLIM43; Fig. 1a). This increase represents ~9% of the recently reported multimodel ensemble mean SMB of 2300 Gt yr⁻¹ and exceeds the standard deviation of 108 Gt yr⁻¹²⁴. We show that most of the additional precipitation occurred over the ice shelves, where the increase in SMB is more pronounced than over grounded land (Supplementary Fig. 1). This suggests that ice shelves act as precipitation sinks or ‘buffer zones’ for moisture transported from further north, with the majority of precipitation reaching the AIS itself being primarily (up to 90%) driven by ARs¹². The frequency of ARs reaching the AP and coastal East Antarctica is indeed significantly higher in the later period (2020–2024) compared to 2003–2019 (Supplementary Fig. 5), and coincides with the regions showing the strongest positive SMB and GMB trends (Fig. 1f, g). Since 2020, only the drainage basins near the Amundsen Sea (Zwally drainage basins 19–21; Supplementary Fig. 9) still have a negative net mass loss due to high rates of dynamical discharge (Fig. 1f, h).

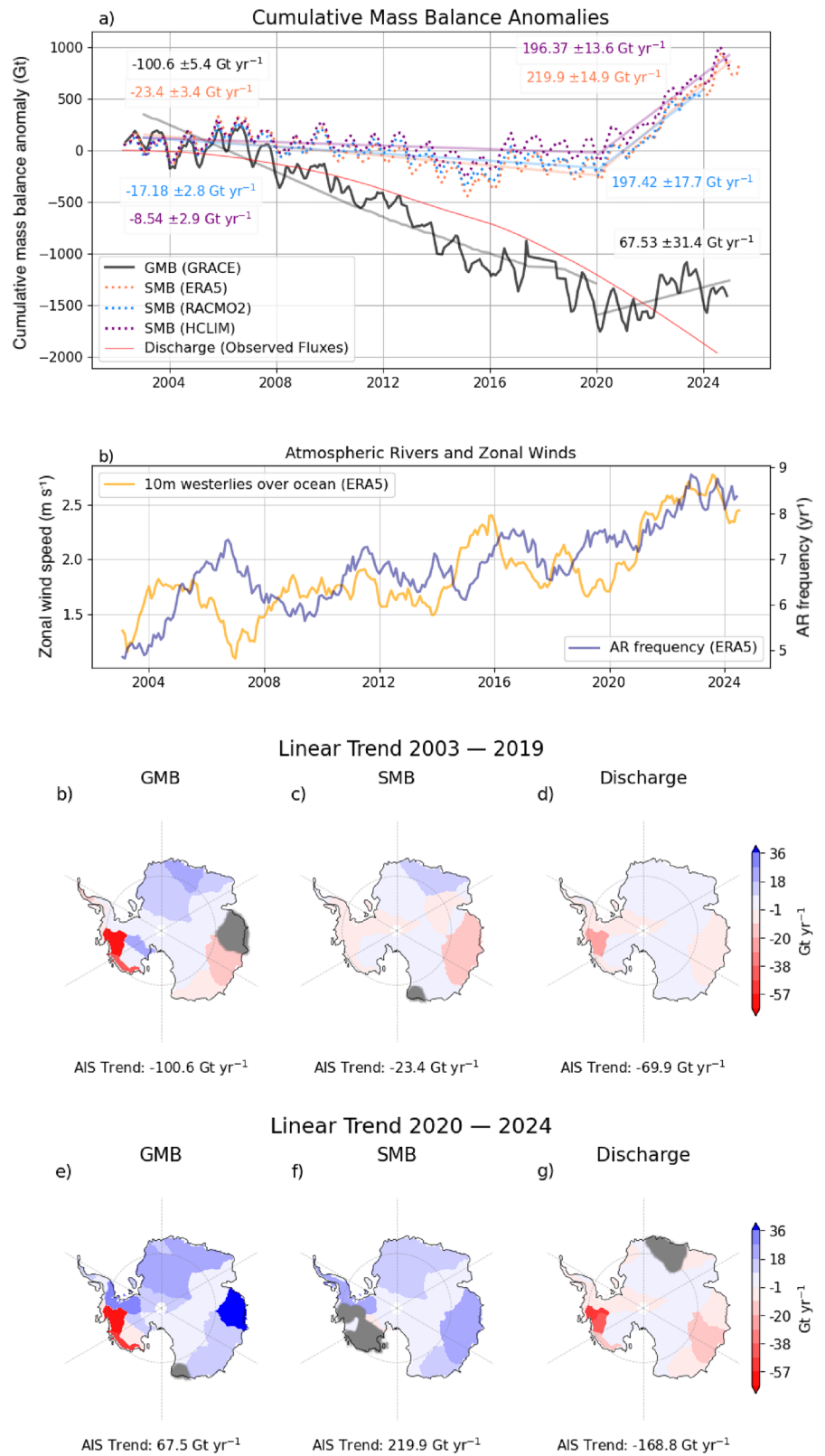
Annual precipitation over the AIS is dominated by short-term, high-impact events, often defined as daily precipitation extremes exceeding the 95th–99th percentile and associated with ARs identified using integrated vapour transport (IVT) percentile thresholds (we use the 95th percentile), which typically produce 1–3-day landfall episodes²⁵. ARs alone are estimated to contribute on average 10–30% of Antarctic precipitation^{9,26,27}. Recent precipitation and SMB increases are evident across most days of the year, particularly during summer (Fig. 2b and Supplementary Fig. 4). This results in a 12.7% higher summer SMB in ERA5 during 2020–2024 (12.2% in HCLIM43; 10% in RACMO2.4p until 2023) compared to the 2003–2019 mean, while winter SMB increased by 7.3% in ERA5 (5.8% in HCLIM43 and 8.4% in RACMO2.4p) (Supplementary Fig. 4).

The summer increase is most pronounced over West Antarctica and the AP, whereas winter SMB has risen mainly along the East Antarctic coastline and tip of the AP. These patterns coincide with regions experiencing the highest AR activity (Supplementary Figs. 5 and 6) and IVT (Supplementary Fig. 7), as well as strengthened westerlies over the past five years (Supplementary Fig. 8 and Fig. 1b), which enhance moisture transport toward the continent and increase the likelihood of (AR-induced) precipitation. Particularly after 2020, both AR frequency and westerly winds intensified, but their strong variability leaves it unclear how long this pattern will continue (Fig. 1b). We find that high AR activity and strengthened zonal winds do not always coincide, and hence their recent synchronisation is likely driving the accelerated increase in Antarctic SMB. Given the relatively short duration (5 years) of increased SMB and AR activity, it remains unclear whether the recent GMB shift marks the onset of a long-term trend. As of April 2025, SMB has not shown signs of declining (Fig. 1a), and continued increases in precipitation are expected under warming, consistent with the Clausius-Clapeyron relation²⁸.

Regional accumulation patterns shaped by SAM, ENSO, and ARs

Previous studies have linked regional variation in Antarctic SMB to different phases of the SAM and the El Niño–Southern Oscillation (ENSO)^{29–34}. Our correlation results for individual sectors (Fig. 3b) align with the finding that the influence of SAM and ENSO on SMB and sea ice is complex and regionally dependent (Fig. 4 and Supplementary Fig. 3). Two dominant patterns emerge: (1) Both modes exert relatively weak influence on East Antarctic SMB and the sea ice in the surrounding ocean basins; and (2) a positive SAM and negative ENSO tend to increase SMB on the AP and reduce it in the Ross Sea sector especially in winter (Fig. 4 and Supplementary Fig. 3), consistent with previous studies^{29,30,33,35}. The concurrent effect of SAM and ENSO on both sea ice and SMB near the AP is also described in an ice core study³¹, which concluded that the anticorrelation between sea ice and SMB is likely not directly driven by sea ice loss, but by their shared response to large-scale atmospheric forcing. The recent sea ice decrease in the Bellingshausen Sea, and the SMB increase on the AP and western Weddell Sea sector (near the Ronne-Filchner Ice Shelf), are thus very likely enhanced by negative ENSO and positive SAM anomalies respectively (Fig. 4 and Supplementary Fig. 3). As the ENSO influence on SMB appears weak during summer, we conclude that the accelerated summer accumulation over the AP and western Weddell Sea sector is largely driven by a positive SAM. This is also supported by the post-2020 alignment of SAM anomalies with Pan-Antarctic time series of SMB (Supplementary Fig. 2). The increased westerlies and deepened Amundsen Sea Low associated with a positive SAM and negative ENSO³⁰ (Supplementary Fig. 2) have favoured more frequent intrusions of north-westerly air masses into the AP (especially in summer), while reducing ARs, IVT and SMB over West Antarctica in winter (Supplementary Figs. 2 and 3). However, SMB and GMB trends over East Antarctica since 2020 are just as strong (Fig. 1f, g), where SAM and ENSO variability alone can not fully explain the enhanced accumulation. While previous studies have shown that SAM and lagged ENSO can have an influence on coastal East Antarctic AR frequency and SMB^{36–38}, the relationship is weaker than in West Antarctica and the peninsula. East Antarctic precipitation is more strongly influenced by synoptic-scale moisture transport from northerly sources, largely due to the higher elevation of the plateau^{10,39}. This explains the lower correlations of

Fig. 1 | Drivers of Antarctic ice sheet mass balance anomalies. **a** Black: Monthly cumulative GMB anomalies from April 2002 to December 2024, based on GRACE (with respect to the mass as of 2011-01-01 before being subtracted from the GMB anomaly in April 2002 to show the changes since the mission launch). Dotted: Monthly cumulative SMB anomalies based on ERA5 from April 2002 to April 2025 (ERA5), December 2024 (HCLIM43) and December 2023 (RACMO2.4p), all with respect to the 1995-2010 mean, before subtracting their SMB from April 2002 (as for GRACE). Light straight solid lines indicate linear trend slopes from 2003 to 2019, and 2020 to 2024 (2023 for RACMO2.4p), with trends printed in the respective colour (all trend slopes are significant with $p < 0.05$). The small change in the grey line's angle around 2017 reflects the 1-year GRACE - GRACE-FO gap. Red time series: Grounding line discharge from³ based on bed topography and velocity measurements from 1996 through to July 2024 (see 'Methods'). **b** AR frequency and 10m zonal winds based on ERA5. Maps below show linear trends of GMB (**c**, **f**), SMB (**d**, **g**), and discharge (**e**, **h**) per basin for the two time periods. Basins are greyed out where the trend is not significant ($p < 0.05$). Drainage basins follow Zwally et al.⁵² as shown in Supplementary Fig. 9⁵².



inland East Antarctic SMB with the climate modes (Supplementary Fig. 3a–f) and local sea ice (Fig. 4 and Supplementary Fig. 10), and suggests that recent episodic AR events have instead increased precipitation in these inland areas, especially during winter (Supplementary Figs. 5d and 6d). That said, sea ice loss can still influence many coastal regions, including parts of East Antarctica¹⁹, both by increasing local heat and humidity fluxes and by

intensifying individual ARs. These mechanisms are examined in the following section.

The role of sea ice in modulating SMB and AR strength

Although large-scale circulation changes are the primary driver of Antarctic precipitation variability in most regions, local sea ice conditions can

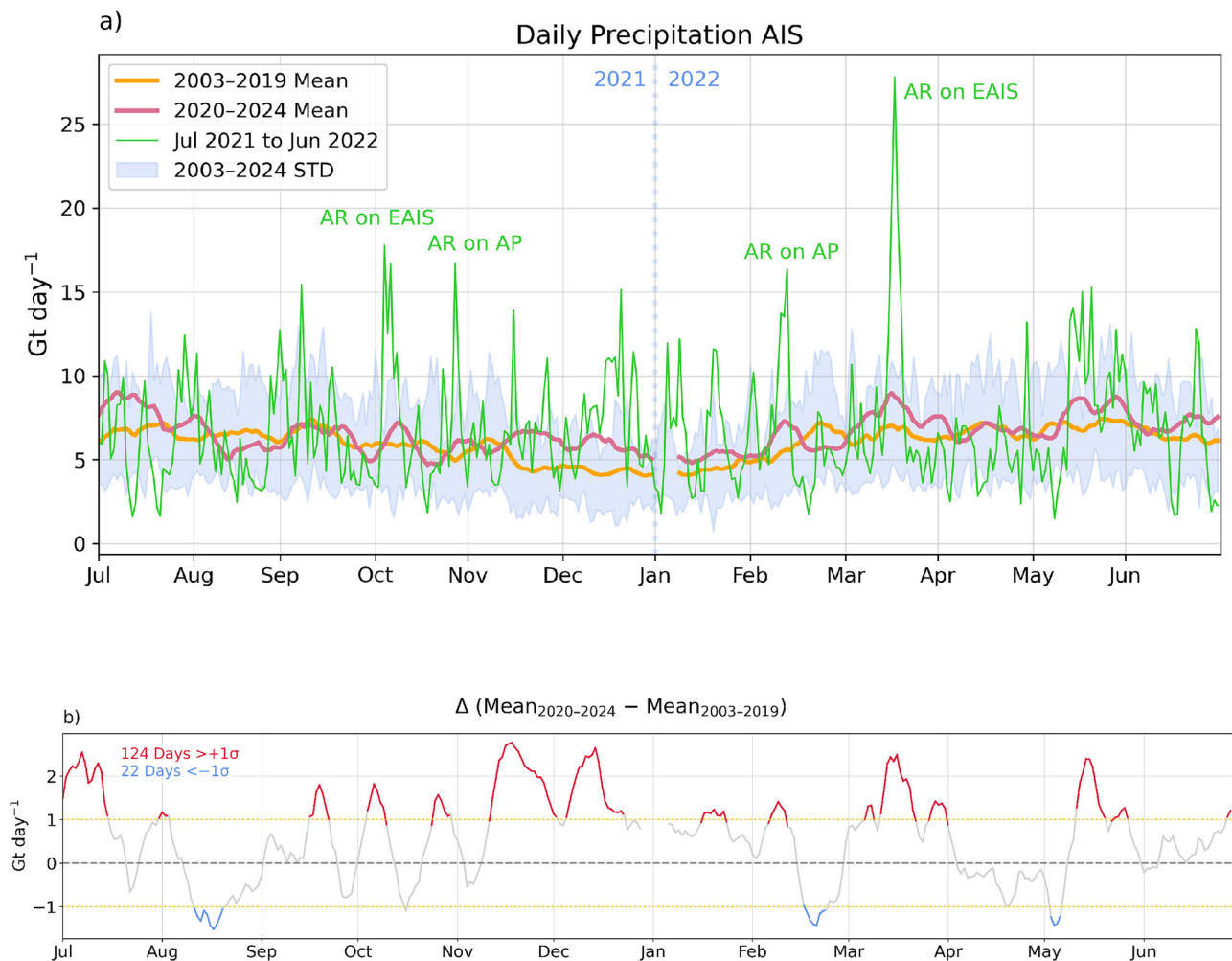


Fig. 2 | Recent increase in Antarctic precipitation. **a** Daily precipitation based on ERA5 over the AIS throughout the year, where the green line represents the example year from Jul 2021 to Jun 2022. Blue shading indicates the daily standard deviation over the full 2003–2024 period. Red and orange line represent the mean daily precipitation (10-day rolling mean) during 2003–2019 and 2020–2024, respectively.

The difference of these two lines (red minus orange) is shown in **(b)**, where red and blue coloured sections mark days where the difference is larger than the standard deviation of the difference (approximately 1 Gt day⁻¹), which is represented by the yellow dotted lines. 124 (22) days are significantly higher (lower) during 2020–2024 compared to 2003–2019.

also strongly affect precipitation by modulating air-sea heat fluxes and moisture availability^{19,40–42}. The fact that Antarctic SIE reached several record lows since 2017 raises questions about a possible linkage between reduced sea ice and enhanced surface accumulation. Local sea ice loss has been shown to contribute to higher precipitation and SMB anomalies over the AIS^{19,43,44} by enhancing sensible and latent heat fluxes to the atmosphere^{40,45}. We find significantly negative correlations between seasonal SIC and SMB, especially during winter and in West Antarctic sectors (Fig. 3 and Supplementary Fig. 10). However, in some regions, such as the Bellingshausen Sea this relationship partly reflects a shared response to large-scale atmospheric forcing³¹. We also find significantly positive SIC-SMB correlations over some ice shelf areas (especially from March to August; Supplementary Fig. 10), which suggests that some of the additional moisture from sea ice loss is precipitated out over the ice shelves before reaching the grounded AIS (this is also supported by our experiments below; Fig. 5f). We repeated the correlations with different time lags (up to 3 months), as well as monthly and annual frequencies, which showed weaker correlations than the seasonal results presented here. Further, Antarctic sea ice began to decline since 2015, several years before the observed shifts in SMB and GMB trends (Fig. 1a). The direct effect of sea ice loss on Antarctic mass gain through locally enhanced evaporation is therefore not insignificant, but unlikely to explain the sudden acceleration in ice sheet-wide precipitation.

To isolate the influence of sea ice on overall Antarctic-wide SMB as well as AR strength, we conducted 1-year idealised simulations from July 2021 to June 2022 with altered SIC (Fig. 5a–c). Figure 2a displays the daily precipitation over the full year and highlights how episodic AR events account for a major share of the total accumulation. All four of the highest precipitation days (>15 Gt day⁻¹) over the AIS during this 1-year period occurred during ARs (Fig. 6a–d).

The conducted RCM simulations with HCLIM43^{18,46} include a control run (CTRL) and two idealised experiments with added sea ice (exICE, where SIC are increased to 100% up to 5° north of the monthly mean SIE), and completely removed sea ice (noICE). The mean SIC of the different experiments over the simulated year are shown in Fig. 5a–c. We note a 249 Gt increase in accumulated grounded AIS precipitation, and a 174 Gt increase in accumulated SMB from July 2021 to June 2022 when comparing noICE to CTRL (Fig. 5d and Supplementary Fig. 11f). Our experiments thus suggest that a completely sea ice-free Southern Ocean during the already low sea ice in 2021/2022 would thus have increased annual grounded ice sheet precipitation by 8.8% and SMB by 7.3% (10.2% and 7% including ice shelves). Directly comparing the two extreme scenarios (exICE and noICE) results in slightly higher values, but here we focus on the changes relative to CTRL. Most additional precipitation from CTRL to noICE falls on ice shelves and coastal areas, where local

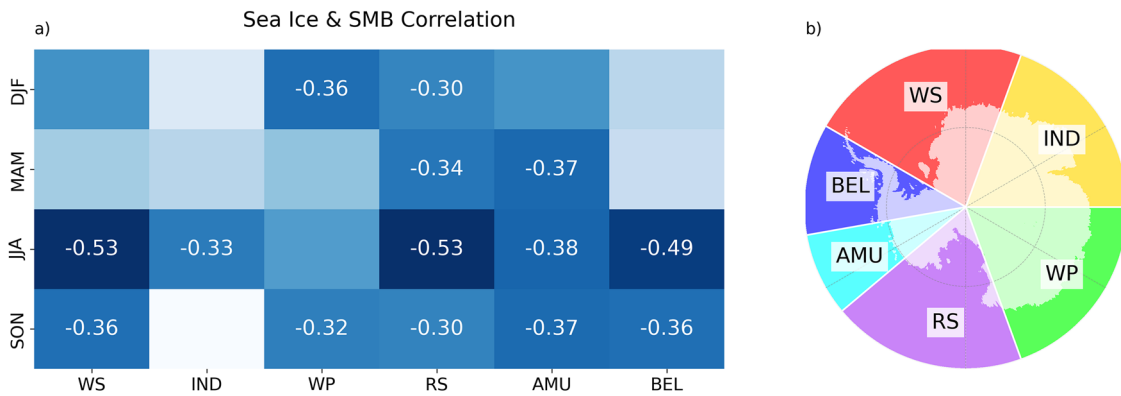


Fig. 3 | Relationship between surface mass balance and sea ice concentration.
a Seasonal correlations of basin-wide SMB and adjacent ocean-basin SIC for summer (DJF), autumn (MAM), winter (JJA), and spring (SON). The basins are shown in **(b)**, where the transparent land areas represent the region where SMB anomalies are summed (excluding ice shelves), and correlated to the respective adjacent ocean

basins. WS Weddell Sea, IND Indian Ocean, WP West Pacific, RS Ross sea, AMU Amundsen sea, BEL Bellingshausen sea. Boxes without numbers indicate insignificant correlations ($p \geq 0.05$). The correlations per grid point are shown in Supplementary Fig. 10. SMB is based on ERA5.

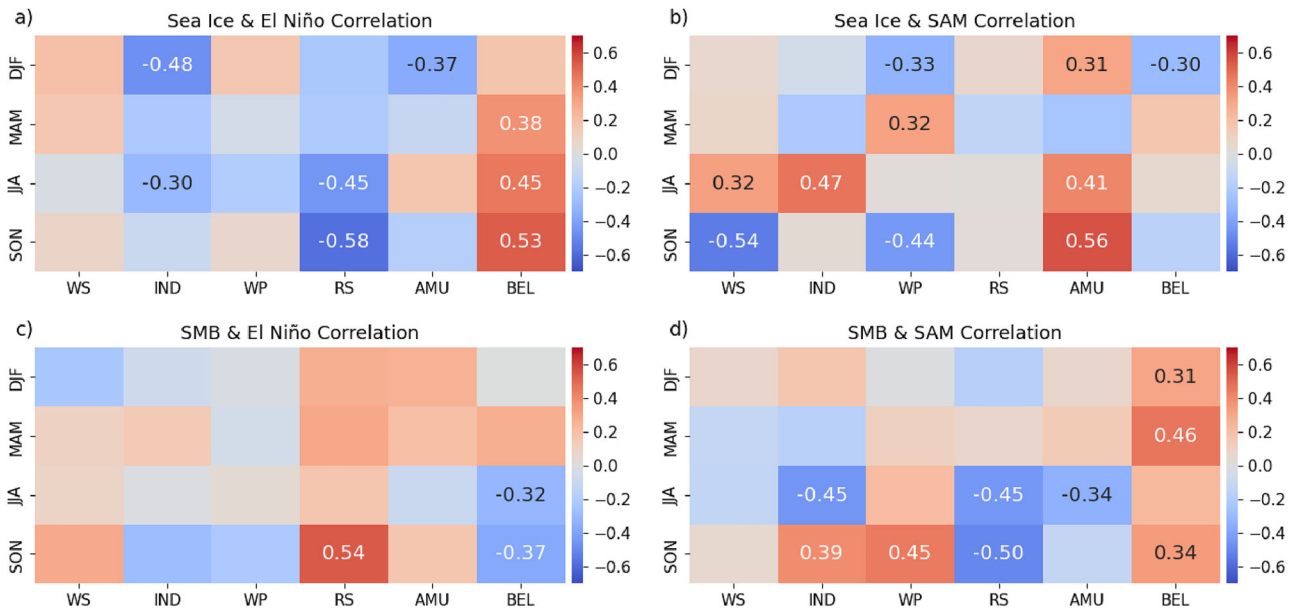


Fig. 4 | Links between sea ice, surface mass balance, and large-scale climate modes. **a, b** Seasonal correlations as in Fig. 3a, but between SIC anomalies in each ocean basin and the large-scale climate modes El Niño (left) and SAM (right),

and **c, d** the same for SMB anomalies over the respective land-covered regions (excluding ice shelves; see Fig. 3b).

precipitation is at some locations increased by as much as 1000 mm yr⁻¹ (Fig. 5f). The areas most affected are Marie Byrd Land, Wilkes Land, and the AP, with over 1700 mm yr⁻¹ of increased precipitation near Larsen C (Fig. 5f). Correspondingly, precipitation is most reduced in these areas if SIC are increased (Fig. 5e).

We also find higher temperatures over the AIS and ice shelves if sea ice is absent, particularly over the Antarctic Peninsula and near the Ross Ice Shelf (Supplementary Fig. 11g–i), where annual mean skin temperatures increase by up to 16 °C. This warming explains why the SMB increase under removed sea ice is smaller than the corresponding increase in precipitation (Supplementary Fig. 11a–c), as a substantially larger portion of land and ice shelf becomes susceptible to evaporation (and runoff, which is not included in our simplified ERA5 and HCLIM43 SMB calculation). The higher land and ice shelf temperatures in the noSIC experiment occur despite lower net downward longwave radiation and turbulent heat fluxes compared to the exICE and CTRL simulations (Supplementary Figs. 13–15). Downward longwave radiation over both ocean and land is increased in noSIC, but this

is outweighed by stronger upward longwave radiation, resulting in a net surface cooling effect from longwave radiation (Supplementary Fig. 13). Instead, higher annual mean land temperatures result primarily from increased net solar radiation (Supplementary Fig. 14) due to lower albedo (Supplementary Fig. 12d–f). Despite increased cloud water content (Supplementary Fig. 12a–c), which lowers downward shortwave absorption, future sea ice loss may therefore increase Antarctic temperatures primarily through reduced shortwave reflection, rather than turbulent fluxes or longwave radiation (though local exceptions exist). We also note a 15.4% increase in land rainfall in noICE (24% decrease in exICE), which is most evident on the AP and Victoria land (Supplementary Fig. 11d–f). Zonal and meridional winds are not significantly affected by the absence or presence of sea ice, suggesting that the recent strengthening of the westerlies (Supplementary Fig. 8) is instead driven by remote, planetary-scale atmospheric forcing.

These atmospheric changes in response to altered SIC are most pronounced during winter (Supplementary Fig. 16g–v), while the impact is

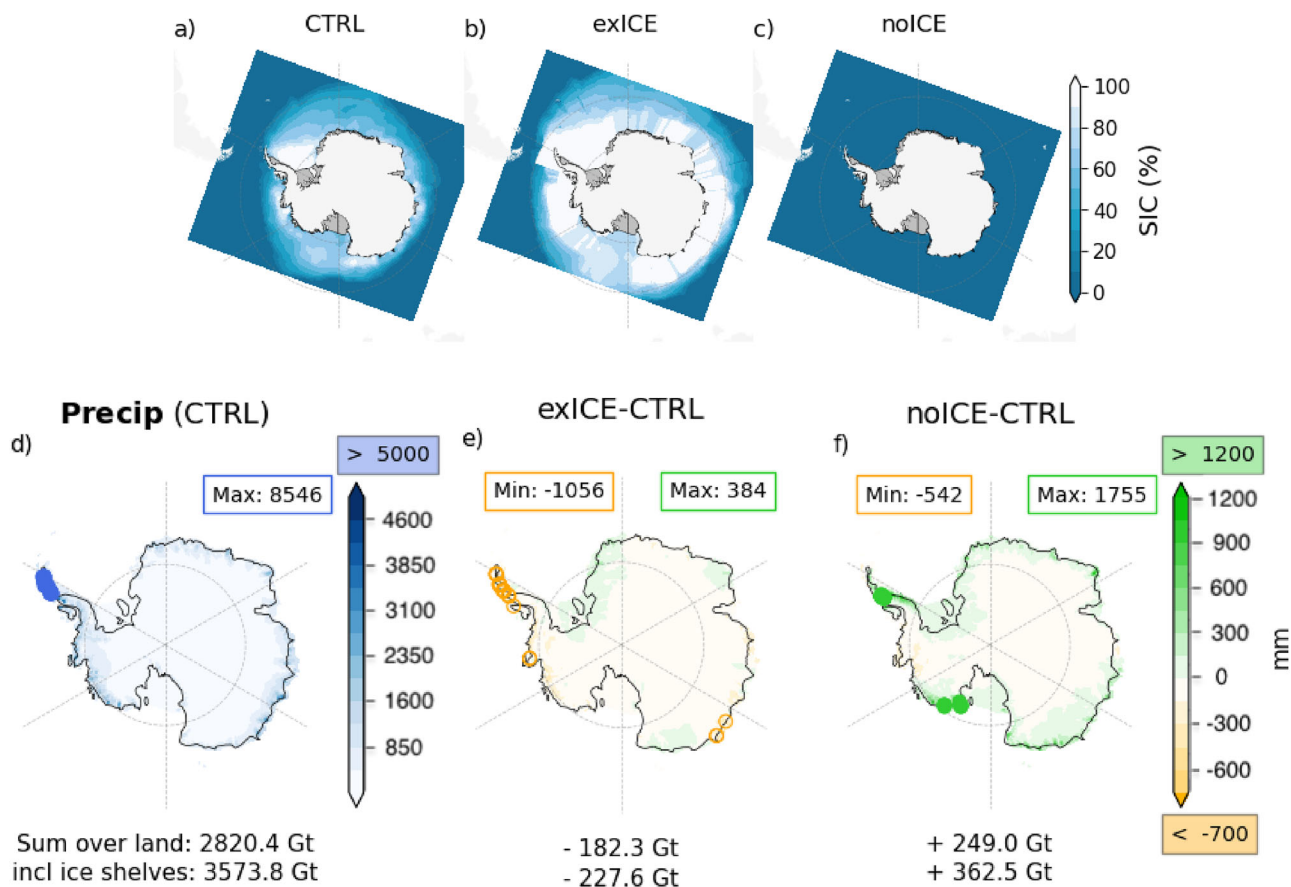


Fig. 5 | Impact of extreme sea ice states on Antarctic precipitation. Mean SIC from June 2021 to July 2022 under (a) control conditions (CTRL), b enhanced sea ice (exICE), and c no sea ice (noICE) scenarios. d Total accumulated precipitation from June 2021 to July 2022 in the control simulation, and that of the noICE (e) and exICE (f) experiments minus the control run. Numbers beneath the plots give the total amount (or difference from) for the grounded ice sheet (AIS) and including ice

shelves (AIS + IS). In d blue circles mark regions exceeding 6000 mm with the maximum value shown in the blue rectangle. In c, d, green circles mark regions exceeding 1500 mm and orange circles mark regions below -1000 mm with min/max values per plot are shown in the upper rectangles; these colour scale limits were chosen to enhance the visibility of spatial patterns in the remaining areas. Respective maps for SMB are shown in Supplementary Fig. 11.

minimal in summer (except for shortwave radiation), when a weaker ocean-air temperature gradient limits evaporation. Since recent mass loss and sea ice loss occurs in both summer and winter, this is further evidence that sea ice loss alone can not explain recent increases in summer SMB. We note a near-linear SMB increase from the exICE over the CTRL to the noICE experiment, with 5.7 (7.3) Gt more SMB per year per million km² of less SIE in summer (winter) over the AIS (Supplementary Fig. 17c). A backward calculation based on SMB and sea ice before and after 2020 suggests that the recent grounded ice sheet SMB increase of 121.9 Gt yr⁻¹ in summer and 78.5 Gt yr⁻¹ in winter (Supplementary Fig. 4) can be attributed by approximately 3.1% and 10.9% to sea ice loss, respectively. This is based on the fact that the mean SIE in the last 5 years was 0.67 million km² lower in summer and 1.17 million km² lower in winter compared to 2002–2019 (in ERA5). On an annual mean, we find that under present-day conditions, every million km² of lost sea ice may result in 11.4 Gt more SMB per year (12.9 Gt including ice shelves) (Supplementary Fig. 17a, b). Annually, the post-2020 trend of 219.9 Gt yr⁻¹ over the grounded AIS (and 340.46 Gt yr⁻¹ including ice shelves), along with 0.82 million km² less sea ice, would indicate an annual 4.3% (or 3.1% with ice shelves) increase due to sea ice loss.

During the four AR events, northerly wind speeds are significantly enhanced at 500 hPa, 850 hPa, and 10 m regardless of SIE (Supplementary Fig. 18). Wind speed magnitudes are similar across experiments at all heights, suggesting that sea ice loss has limited impact on dynamic AR intensification via reduced surface friction or turbulent flux changes, at least in HCLIM43 at 11 km resolution. Still, most events show increased precipitation over land and ice shelves under reduced SIC (Fig. 6f–i). The most

pronounced sea ice effect occurs during the March 2022 heatwave, with over 20 Gt less precipitation across four AR days when sea ice extends to ~60°S (note that the noSIC case shows only a slight precipitation increase due to already low ice extent in the CTRL). In contrast, the AP heatwave in 2022 shows minimal sensitivity, likely because sea ice was already sparse (Supplementary Fig. 19g). Across all cases, spatial analyses reveal a complex atmospheric response to the altered SIC, caused by displaced frontal boundaries and convergence zones (Supplementary Fig. 19).

Conclusions

We conclude that the recent increase in AIS mass is primarily driven by stronger westerlies and more frequent ARs. The SMB and AR increases are strongest in summer, especially on the AP and the western Weddell Sea sector, associated with a positive SAM. Winter SMB has increased along most of the Antarctic coast except for West Antarctica, and we estimate that sea ice loss contributed ~11% of the recent winter SMB increase (~3% in summer). Together, these remote and local thermodynamic and circulation changes increased SMB enough to offset continued ice discharge losses. Our findings also show that most of the additional uptake of moisture during ARs over a sea ice-free Southern Ocean is lost locally or on ice shelves, while the strength of the higher-elevation moisture flow during ARs is largely unaffected by sea ice. Our experiments still confirm that Antarctic SMB does increase due to sea ice loss, even if relatively small, and we note that larger SST increases than imposed here could lead to more precipitation (and also enhanced ice melt). More important questions remain regarding the role of climate change in modifying

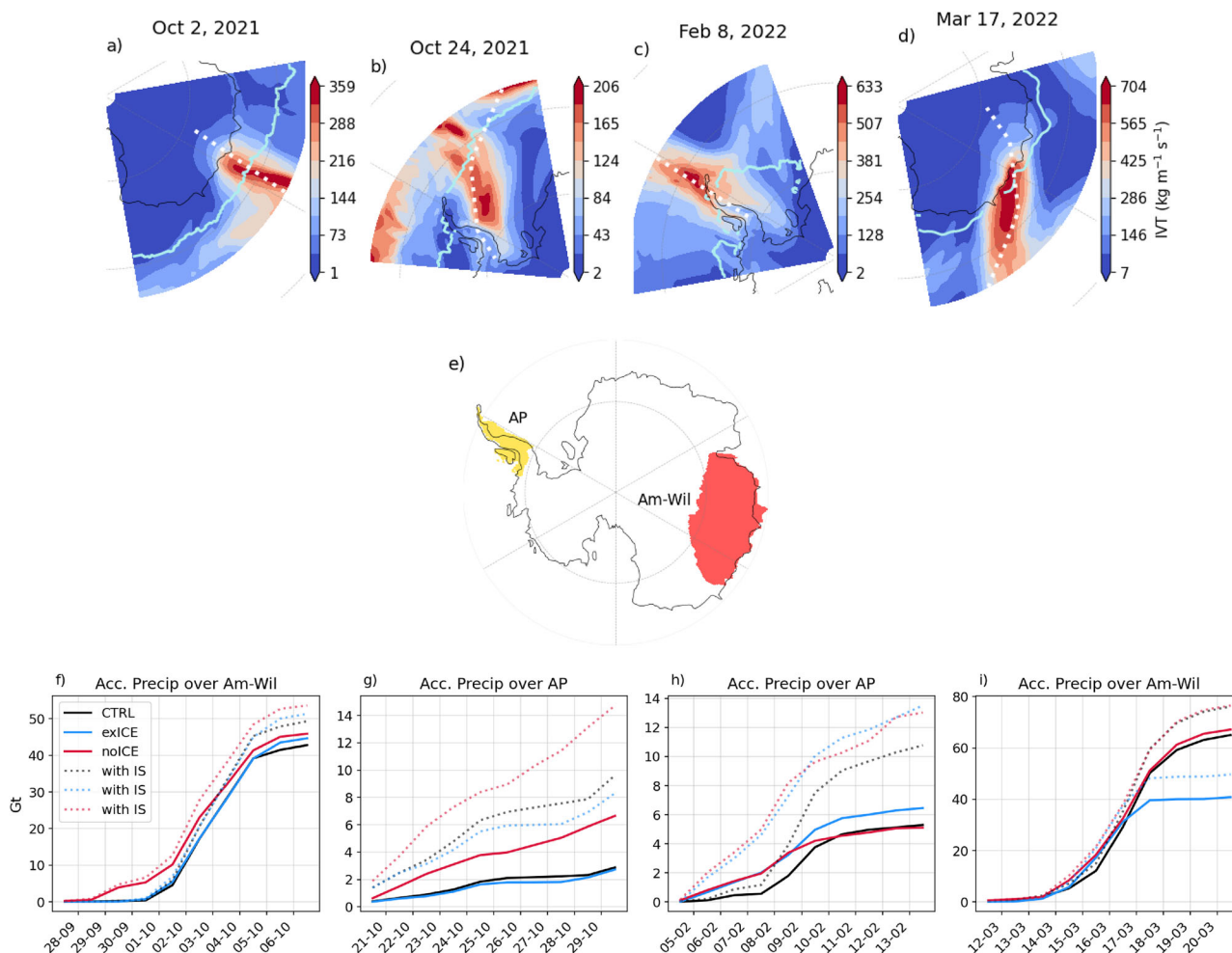


Fig. 6 | Atmospheric river events in sea ice sensitivity experiments. a–d AR events included in the 1-year sea ice experiments with HCLIM43. Here data is based on ERA5; the light blue solid line shows the sea ice edge, and the white dotted line indicates the AR axis cross-sections. e Drainage basins which were most affected by

the four ARs: the Antarctic Peninsula (AP), and Amery-and-Wilkes Land (Am-Wil). The 10-day time series below f–i shows the accumulated precipitation for each event and experiment on the grounded ice sheet (solid lines) and that including ice shelves (dotted lines).

precipitation and surface melt from ARs in Antarctica, with significant implications for future sea level rise estimates.

Methods

Gravitational mass balance

AIS mass balance can be estimated using various methods, including ice accumulation combined with ice velocity and thickness derived from satellite radar and optical imagery, altimetry (radar or laser), or gravimetry. These methods generally yield consistent results at the large scale^{47,48}. GMB trends estimates can differ greatly across studies, due to different data sources, corrections applied, slightly different time periods (e.g. Table 3 in ref. 6 or⁴⁹). Gravimetry data from the GRACE satellite mission, launched in 2002 (and its successor GRACE-FO, both referred to as GRACE hereafter), provide estimates of AIS mass change, after corrections for the Earth’s shape⁵⁰ and glacial isostatic adjustment (GIA)⁵¹.

We use the ESA CCI AIS Gravimetric Mass Balance Gridded Product (v5.0), provided by TU Dresden, derived from GRACE/GRACE-FO Level-2 monthly solutions from the Center for Space Research (CSR, RL06.3), which provides a time series of gridded as well as drainage basin-specific ice mass changes over Antarctica defined by Zwally et al.⁵². The dataset also applies a GIA correction using the IJ05_R2 model⁵¹ and accounts for ellipsoidal corrections⁵⁰. It has a spatial resolution of 350 km with a $50 \times 50 \text{ km}^2$ grid and covers the period April 2002 to December 2024. Ice mass changes are referenced to 2011-01-01 based on a linear,

periodic (annual and semi-annual), and quadratic fit to monthly solutions over 2002-08 to 2016-08. We subtracted all GMB anomalies from the GMB anomaly of April 2002 to show the mass loss since 2002 in line with the SMB data (Fig. 1a).

Surface mass balance

We use precipitation and evaporation fields from ERA5⁵³ to estimate SMB from 1985 to April 2025, calculated as precipitation minus evaporation and sublimation. Although additional processes influence the final SMB, this provides a close approximation when compared with more advanced SMB estimates²³. ERA5 shows reasonable performance for Antarctic climate and synoptic systems⁵⁴⁻⁵⁶, and offers relatively high horizontal resolution compared to other reanalyses (31 km). We also use simulations from HCLIM43⁴⁶ in the AROME configuration at 11 km resolution (downscaled from ERA5), for which SMB is likewise computed as precipitation minus evaporation and sublimation.

To compare ERA5 SMB to more sophisticated SMB calculations, we further use updated RACMO2.4p SMB data on 11 km grids from 1985 to 2023⁵⁷. RACMO2.4p estimates SMB as the sum of snowfall, rainfall, sublimation, drifting snow erosion, and meltwater runoff, using a multi-layer snow scheme that includes snow densification, melt percolation, and refreezing. The model is driven by ERA5 reanalysis at the lateral boundaries and incorporates updated IFS physics, including prognostic precipitation types and a spectral snow albedo scheme coupled to the TARTES radiative

transfer model. Snow processes specific to polar conditions, such as blowing snow and superimposed ice formation, are explicitly represented.

SMB anomalies for all SMB data are derived by subtracting the 1995–2010 mean (as 1995 was the first time step for HCIM).

Atmospheric rivers

Two AR algorithms/catalogues were used to evaluate changes in AR frequency and AR precipitation: The algorithm for AIS Atmospheric Rivers (ANTIS-AR; developed here) and the ERA5-based Dataset for Atmospheric River Analysis (EDARA)⁵⁸, which both use IVT from ERA5. For ANTIS-AR we use the vertical integrals of eastward (F_u) and northward (F_v) water vapour fluxes, which represent the total column-integrated moisture flux (in $\text{kg m}^{-1} \text{s}^{-1}$) from the surface to the top of the atmosphere. IVT is then calculated as

$$\text{IVT} = \sqrt{F_u^2 + F_v^2} \quad (1)$$

F_u and F_v are derived internally by ECMWF from model-level winds and specific humidity as

$$F_u, F_v = -\frac{1}{g} \int_{p_{\text{sic}}}^{p_{\text{top}}} (u, v) q \, dp \quad (2)$$

where u and v are the horizontal wind components, q is specific humidity, p is pressure, g is gravitational acceleration, and p_{sic} and p_{top} (~ 0.1 hPa) correspond to the surface pressure and the top of the model atmosphere. We preferred this method to integrating pressure-level data because ERA5 extrapolates humidity and wind fields to the surface, which, if not adjusted to actual surface pressure, can lead to overestimation of IVT⁵⁹.

The ANTIS-AR algorithm was specifically developed for this study to identify extreme zonal and meridional ARs that make landfall on the ice sheet and/or shelves. It detects contiguous regions where IVT exceeds the 95th percentile of the monthly climatological IVT $_{u,v}$ at each grid point, with a minimum IVT threshold of $40 \text{ kg m}^{-1} \text{ s}^{-1}$. Identified regions must have a length-to-width ratio of at least 2:1⁶⁰ and a minimum length of 1300 km. We reduced this threshold from the more common global definitions of 1500 or 2000 km, as we only evaluated IVT fields south of 60°S (i.e. ARs extending farther north are truncated). ARs were detected on the original 25 km grid and daily time steps. A 1-year sensitivity analysis for 2024 revealed a negligible increase in AR frequency (from 6.24 to 6.36 AR days yr^{-1} on average) if detected on 12-h time steps.

EDARA⁵⁸ is a global ERA5-based AR dataset that follows the detection framework of Guan et al.⁶¹. It is not specifically optimised for polar regions (e.g. it uses a relatively high IVT threshold of $100 \text{ kg m}^{-1} \text{ s}^{-1}$), but provides a valuable baseline to compare AR changes detected using our ANTIS-AR algorithm. EDARA detects ARs that exceed the 85th percentile of IVT $_{u,v}$ and is therefore technically less strict than ANTIS-AR. However, because the absolute IVT threshold of $100 \text{ kg m}^{-1} \text{ s}^{-1}$ must also be exceeded (which is rarely the case over Antarctica even during strong ARs), EDARA tends to underestimate AR frequency and extent over the AIS, but detects more ARs over the surrounding Southern Ocean. The used EDARA-ARs in this study are based on the mtARget-v3 algorithm, which improves the identification of zonally oriented ARs. Since this study focuses on ARs affecting land and ice shelves, only EDARA ARs that reach at least one grid cell of land or ice shelf are considered.

HCLIM43 experiments

The sea ice experiment simulations (CTRL, exICE and noICE; see Methods) were performed using the non-hydrostatic RCM HCLIM-AROME, version 43⁴⁶, at 11 km resolution. An overview of the model physics used in HCLIM43-AROME is summarised below, and the domain boundaries are shown in Fig. 5a.

The model employs a non-hydrostatic dynamical core with deep convection explicitly resolved. Shallow convection is parameterised using

the EDMFm scheme^{62,63}, which incorporates a dual mass-flux framework to represent both dry and moist updrafts⁶⁴. Cloud processes are simulated using the statistical cloud scheme of Bechtold et al.⁶⁵. Microphysics follow the ICE3 single-moment bulk scheme⁶⁶, predicting cloud water, rain, cloud ice, snow, and graupel. For cold conditions, ICE3 is used with the OCND2 modifications⁶⁷, which improve the representation of supercooled liquid water, fog, and mixed-phase cloud layers. Radiative transfer is handled using RRTM for longwave radiation^{68,69} and the six-band SW6 shortwave scheme⁷⁰, a simplified version of the ECMWF radiation scheme⁷¹. Turbulence is represented using the HARATU scheme^{63,72}. Surface processes are represented with the land-surface model SURFEX⁷³, which simulates snow on ice using the 12-layer Interactions Surface Biosphere Atmosphere Explicit Snow (ISBA-ES) model⁷⁴. The topmost snow layer is always ≤ 0.05 m thick, and the scheme calculates snow thermal conductivity, radiative fluxes, accumulation, melt, and compaction across the full multilayer snowpack. Snow albedo is computed following the CROCUS method^{75,76} in three spectral bands ([0.3–0.8], [0.8–1.5], and [1.5–2.8] μm), which are combined to provide total broadband albedo. The default albedo varies with snow density, optical grain size, and snow aging and sea ice thermodynamics are treated using the SICE module, which solves heat diffusion through a prescribed ice layer and couples to the overlying multilayer ISBA-3L snow scheme to represent vertical temperature gradients, metamorphism, accumulation, melt, and compaction. The ice sheet mask was derived from BedMachine Antarctica⁷⁷. The snow and ice internal physical conditions over the ice sheet were initialised according to the SURFEX/ISBA-ES land-surface scheme, which simulates the thermal and physical properties of the snow and ice layers (including snow temperature, density, compaction, and optical grain size)^{73,74}.

HCLIM43-AROME was driven by ERA5 at the lateral boundaries and ocean surface (temperature, zonal and meridional winds, specific humidity, SIC, SST and surface pressure) with 3-hourly updates. Nudging was applied to air temperature, divergence and vorticity above 850 hPa, with a length scale of approximately 800 km (moisture fields were excluded). The downscaling experiment was run from July 2021 to June 2022, with one month of spin-up (Torres-Alavez et al.; in preparation).

In the noICE experiment, the SSTs over areas originally covered by sea ice represent SSTs from ERA5 (below the sea ice cover), and the albedo was set to that of the open ocean (0.07–0.09).

In the exICE experiment, where SIC is increased to 100% up to 5° north of the monthly mean SIE, the sea ice surface temperature is computed interactively by the thermodynamic sea ice scheme, SICE, implemented in HCLIM. SICE calculates the temperature profile within the ice by solving the heat-diffusion equation through a slab of prescribed thickness. SICE explicitly couples the ice to the snow layer through heat and momentum fluxes at the snow-ice interface. We chose 5° north of the monthly mean ice edge to represent a physically plausible but substantial perturbation to the sea ice boundary (see Fig. 5a)⁷⁸.

For all experiments (CTRL, exICE and noICE), we use ERA5 as lateral boundary conditions. This allows us to isolate the local atmospheric response but means that the large-scale atmospheric state is constrained for the two extreme perturbations.

SAM and ENSO

To analyse the impact of variability of planetary climate modes, we used the SAM and ENSO indices provided at <http://www.nerc-bas.ac.uk/icd/gjma/sam.html> and https://ds.data.jma.go.jp/tcc/tcc/products/el_nino/index/ respectively. As there are different types of El Niños, we focused on the two main ones: El Niño3 and El Niño4, which we averaged in this study, as the time series are very comparable. We also did sensitivity test of SMB and El Niño3 and El Niño4 indices separately, which resulted in very similar results (e.g. Supplementary Fig. 3).

Data availability

Data for the three different HCLIM43 experiments have been uploaded to [https://ensemblesrt3.dmi.dk/data/prudence/temp/JAT/Marlen/year/\(CTL](https://ensemblesrt3.dmi.dk/data/prudence/temp/JAT/Marlen/year/(CTL)

denotes the control simulation, WICE represents the idealised experiment with added sea ice, and NICE the experiment with completely removed sea ice; subfolders are ordered by month from June 2021 to July 2022). Gravitational mass balance data was sourced from https://data1.geo.tu-dresden.de/ais_gmb/, where GRACE/GRACE-FO L2 monthly solutions are provided by the Center for Space Research (CSR RL06.2). RACMO2.4p-based SMB is provided at <https://zenodo.org/records/14217232>. ERA5 meteorological fields were retrieved via the Climate Data Store (CDS) infrastructure <https://cds.climate.copernicus.eu/datasets/reanalysis-era5-complete?tab=overview>. Grounding line discharge estimates are available at <https://doi.org/10.5281/zenodo.10051893>⁸. Indices for SAM and ENSO (El Niño 3&4 SST anomalies) are provided at <http://www.nerc-bas.ac.uk/icd/gjma/sam.html> and <https://ds.data.jma.go.jp/tcc/tcc/products/elnino/index/> respectively.

Code availability

Python scripts for the AR detection algorithm for ANTIS-AR as well as the code for filtering ARs from EDARA that reach the Antarctic ice sheet or shelves can be accessed via <https://doi.org/10.5281/zenodo.15645442>. The EDARA IVT and AR detection scripts by Mo (2024) are available at <https://www.frdr-dfdr.ca/repo/dataset/b1798e59-b38e-4a83-ab88-12d0a8aca28f>.

Received: 17 September 2025; Accepted: 19 January 2026;

Published online: 03 February 2026

References

- Purich, A. & England, M. H. Projected impacts of Antarctic meltwater anomalies over the twenty-first century. *J. Clim.* **36**, 2703–2719 (2023).
- Li, Q., England, M. H., Hogg, A. M., Rintoul, S. R. & Morrison, A. K. Abyssal ocean overturning slowdown and warming driven by Antarctic meltwater. *Nature* **615**, 841–847 (2023).
- Ferrari, R. et al. Antarctic sea ice control on ocean circulation in present and glacial climates. *Proc. Natl. Acad. Sci. USA* **111**, 8753–8758 (2014).
- Berk, J. vd, Drijfhout, S. & Hazeleger, W. Circulation adjustment in the arctic and atlantic in response to Greenland and Antarctic mass loss. *Clim. Dyn.* **57**, 1689–1707 (2021).
- Wang, W., Shen, Y., Chen, Q. & Wang, F. Unprecedented mass gain over the antarctic ice sheet between 2021 and 2022 caused by large precipitation anomalies. *Environ. Res. Lett.* **18**, 124012 (2023).
- Zhang, R., Xu, M., Che, T., Guo, W. & Li, X. Ice sheet mass changes over antarctica based on GRACE data. *Remote Sens.* **16**, 3776 (2024).
- Ekaykin, A. A., Veres, A. N. & Wang, Y. Recent increase in the surface mass balance in central east antarctica is unprecedented for the last 2000 years. *Commun. Earth Environ.* **5**, 200 (2024).
- Davison, B. J., Hogg, A. E., Slater, T. & Rigby, R. Antarctic ice sheet grounding line discharge from 1996 through 2023. *Earth Syst. Sci. Data Discuss.* **2023**, 1–35 (2023).
- Li, J. et al. Unraveling the contributions of atmospheric rivers on Antarctica crustal deformation and its spatiotemporal distribution during the past decade. *Geophys. J. Int.* **235**, 1325–1338 (2023).
- Dalaiden, Q., Goosse, H., Lenaerts, J. T., Cavitte, M. G. & Henderson, N. Future antarctic snow accumulation trend is dominated by atmospheric synoptic-scale events. *Commun. Earth Environ.* **1**, 62 (2020).
- Nash, D., Waliser, D., Guan, B., Ye, H. & Ralph, F. M. The role of atmospheric rivers in extratropical and polar hydroclimate. *J. Geophys. Res.* **123**, 6804–6821 (2018).
- Wille, J. D. et al. Atmospheric rivers in Antarctica. *Nat. Rev. Earth Environ.* **6**, 178–192 (2025).
- Gorodetskaya, I. V. et al. Record-high Antarctic Peninsula temperatures and surface melt in February 2022: a compound event with an intense atmospheric river. *npj Clim. Atmos. Sci.* **6**, 202 (2023).
- Zou, X. et al. Strong warming over the antarctic peninsula during combined atmospheric river and foehn events: contribution of shortwave radiation and turbulence. *J. Geophys. Res.* **128**, e2022JD038138 (2023).
- Wille, J. D. et al. The extraordinary march 2022 east antarctica “heat” wave. part i: observations and meteorological drivers. *J. Clim.* **37**, 757–778 (2024).
- Wille, J. D. et al. The extraordinary march 2022 east antarctica “heat” wave. part ii: impacts on the antarctic ice sheet. *J. Clim.* **37**, 779–799 (2024).
- Blanchard-Wrigglesworth, E., Cox, T., Espinosa, Z. I. & Donohoe, A. The largest ever recorded heatwave—characteristics and attribution of the Antarctic heatwave of March 2022. *Geophys. Res. Lett.* **50**, e2023GL104910 (2023).
- Kolbe, M. et al. Model performance and surface impacts of atmospheric river events in antarctica. *Discov. Atmos.* **3**, 4 (2025).
- Kittel, C. et al. Sensitivity of the current antarctic surface mass balance to sea surface conditions using MAR. *Cryosphere* **12**, 3827–3839 (2018).
- Groh, A. & Horwath, M. Antarctic ice mass change products from GRACE/GRACE-FO using tailored sensitivity kernels. *Remote Sens.* **13**, 1736 (2021).
- Velicogna, I. et al. Continuity of ice sheet mass loss in Greenland and Antarctica from the GRACE and GRACE Follow-On missions. *Geophys. Res. Lett.* **47**, e2020GL087291 (2020).
- Loomis, B., Luthcke, S. & Sabaka, T. Regularization and error characterization of GRACE mascons. *J. Geod.* **93**, 1381–1398 (2019).
- Wang, X. et al. Comparing surface mass balance and surface temperatures from regional climate models and reanalyses to observations over the Antarctic ice sheet. *Int. J. Climatol.* **45**, e8767 (2025).
- Mottram, R. et al. What is the surface mass balance of Antarctica? An intercomparison of regional climate model estimates. *Cryosphere* **15**, 3751–3784 (2021).
- Gorodetskaya, I. V. et al. The role of atmospheric rivers in anomalous snow accumulation in East Antarctica. *Geophys. Res. Lett.* **41**, 6199–6206 (2014).
- Maclennan, M. L., Lenaerts, J. T., Shields, C. & Wille, J. D. Contribution of atmospheric rivers to Antarctic precipitation. *Geophys. Res. Lett.* **49**, e2022GL100585 (2022).
- Wille, J. D. et al. Antarctic atmospheric river climatology and precipitation impacts. *J. Geophys. Res.* **126**, e2020JD033788 (2021).
- Nicola, L., Notz, D. & Winkelmann, R. Revisiting temperature sensitivity: how does Antarctic precipitation change with temperature? *Cryosphere* **17**, 2563–2583 (2023).
- Medley, B. et al. Temperature and snowfall in western queen maud land increasing faster than climate model projections. *Geophys. Res. Lett.* **45**, 1472–1480 (2018).
- Wang, J. et al. The impacts of combined SAM and ENSO on seasonal Antarctic sea ice changes. *J. Clim.* **36**, 3553–3569 (2023).
- Porter, S. E., Parkinson, C. L. & Mosley-Thompson, E. Bellingshausen sea ice extent recorded in an Antarctic Peninsula ice core. *J. Geophys. Res.* **121**, 13–886 (2016).
- Macha, J. et al. Distinct central and eastern Pacific El Niño influence on antarctic surface mass balance. *Geophys. Res. Lett.* **51**, e2024GL109423 (2024).
- Vannitsem, S., Dalaiden, Q. & Goosse, H. Testing for dynamical dependence: Application to the surface mass balance over antarctica. *Geophys. Res. Lett.* **46**, 12125–12135 (2019).
- Wang, S. et al. Strong impact of the rare three-year La Niña event on Antarctic surface climate changes in 2021–2023. *npj Clim. Atmos. Sci.* **8**, 173 (2025).
- Bodart, J. & Bingham, R. The impact of the extreme 2015–2016 el niño on the mass balance of the Antarctic ice sheet. *Geophys. Res. Lett.* **46**, 13862–13871 (2019).
- King, M. A., Lyu, K. & Zhang, X. Climate variability a key driver of recent antarctic ice-mass change. *Nat. Geosci.* **16**, 1128–1135 (2023).

37. Shields, C. A., Wille, J. D., Marquardt Collow, A. B., Maclennan, M. & Gorodetskaya, I. V. Evaluating uncertainty and modes of variability for antarctic atmospheric rivers. *Geophys. Res. Lett.* **49**, e2022GL099577 (2022).
38. Pohl, B. et al. Relationship between weather regimes and atmospheric rivers in east antarctica. *J. Geophys. Res.* **126**, e2021JD035294 (2021).
39. Bailey, A., Singh, H. K. & Nusbaumer, J. Evaluating a moist isentropic framework for poleward moisture transport: implications for water isotopes over antarctica. *Geophys. Res. Lett.* **46**, 7819–7827 (2019).
40. Trusel, L. D., Kromer, J. D. & Datta, R. T. Atmospheric response to antarctic sea-ice reductions drives ice sheet surface mass balance increases. *J. Clim.* **36**, 6879–6896 (2023).
41. Josey, S. A. et al. Record-low Antarctic sea ice in 2023 increased ocean heat loss and storms. *Nature* **636**, 635–639 (2024).
42. Kromer, J. D. & Trusel, L. D. Identifying the impacts of sea ice variability on the climate and surface mass balance of west antarctica. *Geophys. Res. Lett.* **50**, e2023GL104436 (2023).
43. Wang, H. et al. Influence of sea-ice anomalies on Antarctic precipitation using source attribution in the Community Earth System Model. *Cryosphere* **14**, 429–444 (2020).
44. Sodemann, H. & Stohl, A. Asymmetries in the moisture origin of Antarctic precipitation. *Geophys. Res. Lett.* **36**, 22 (2009).
45. Hofsteenge, M., Cullen, N., Sodemann, H. & Taturji, M. Synoptic drivers and moisture sources of snowfall in coastal Victoria Land, Antarctica. *J. Geophys. Res.* **130**, e2024JD042021 (2025).
46. Belušić, D. et al. Hclim38: a flexible regional climate model applicable for different climate zones from coarse to convection-permitting scales. *Geosci. Model Dev.* **13**, 1311–1333 (2020).
47. Shepherd, A. et al. A reconciled estimate of ice-sheet mass balance. *Science* **338**, 1183–1189 (2012).
48. Otosaka, I. N. et al. Mass balance of the Greenland and Antarctic ice sheets from 1992 to 2020. *Earth Syst. Sci. Data Discuss.* **2022**, 1–33 (2022).
49. Döhne, T., Horwath, M., Groh, A. & Buchta, E. The sensitivity kernel perspective on grace mass change estimates. *J. Geod.* **97**, 11 (2023).
50. Ditmar, P. Conversion of time-varying Stokes coefficients into mass anomalies at the Earth's surface considering the Earth's oblateness. *J. Geod.* **92**, 1401–1412 (2018).
51. Ivins, E. R. et al. Antarctic contribution to sea level rise observed by grace with improved gia correction. *J. Geophys. Res.* **118**, 3126–3141 (2013).
52. Zwally, H. J. et al. Mass gains of the Antarctic ice sheet exceed losses. *J. Glaciol.* **61**, 1019–1036 (2015).
53. Hersbach, H. et al. The era5 global reanalysis. *Q. J. R. Meteorol. Soc.* **146**, 1999–2049 (2020).
54. Gossart, A. et al. An evaluation of surface climatology in state-of-the-art reanalyses over the Antarctic ice sheet. *J. Clim.* **32**, 6899–6915 (2019).
55. McDonald, A. J. & Cairns, L. H. A new method to evaluate reanalyses using synoptic patterns: an example application in the Ross Sea/Ross ice shelf region. *Earth Space Sci.* **7**, e2019EA000794 (2020).
56. Gorodetskaya, I. V., Silva, T., Schmithüsen, H. & Hirasawa, N. Atmospheric river signatures in radiosonde profiles and reanalyses at the Dronning Maud Land coast, East Antarctica. *Adv. Atmos. Sci.* **37**, 455–476 (2020).
57. van Dalum, C. T., van de Berg, W. J., van den Broeke, M. R. & van Tiggelen, M. The surface mass balance and near-surface climate of the Antarctic ice sheet in racmo2. 4p1. *EGUsphere* **2025**, 1–40 (2025).
58. Mo, R. Edara: an era5-based dataset for atmospheric river analysis. *Sci. Data* **11**, 900 (2024).
59. Kolbe, M., Bintanja, R., van der Linden, E. C. & Cordero, R. R. Vertical structure and surface impact of atmospheric rivers reaching Antarctic sea ice and land. *Atmos. Res.* **315**, 107841 (2025).
60. Simmonds, I., Keay, K. & Tristram Bye, J. A. Identification and climatology of southern hemisphere mobile fronts in a modern reanalysis. *J. Clim.* **25**, 1945–1962 (2012).
61. Guan, B. & Waliser, D. E. Detection of atmospheric rivers: Evaluation and application of an algorithm for global studies. *J. Geophys. Res.* **120**, 12514–12535 (2015).
62. De Rooy, W. C. et al. Model development in practice: a comprehensive update to the boundary layer schemes in HARMONIE-AROME cycle 40. *Geosci. Model Dev.* **15**, 1513–1543 (2022).
63. Bengtsson, L. et al. The harmonie–arome model configuration in the ALADIN–HIRLAM NWP system. *Mon. Weather Rev.* **145**, 1919–1935 (2017).
64. Neggers, R. A., Köhler, M. & Beljaars, A. C. A dual mass flux framework for boundary layer convection. Part I: transport. *J. Atmos. Sci.* **66**, 1465–1487 (2009).
65. Bechtold, P., Cuijpers, J., Mascart, P. & Trouilhet, P. Modeling of trade wind cumuli with a low-order turbulence model: toward a unified description of cu and se clouds in meteorological models. *J. Atmos. Sci.* **52**, 455–463 (1995).
66. Pinty, J.-P. & Jabouille, P. A mixed-phase cloud parameterization for use in mesoscale non-hydrostatic model: simulations of a squall line and of orographic precipitations. In *Proc. Conference on Cloud Physics* 217–220 (1998).
67. Müller, M. et al. Arome-metcoop: a nordic convective-scale operational weather prediction model. *Weather Forecast.* **32**, 609–627 (2017).
68. Mlawer, E. J., Taubman, S. J., Brown, P. D., Iacono, M. J. & Clough, S. A. Radiative transfer for inhomogeneous atmospheres: Rrtm, a validated correlated-k model for the longwave. *J. Geophys. Res.* **102**, 16663–16682 (1997).
69. Iacono, M. J., Mlawer, E. J., Clough, S. A. & Morcrette, J.-J. Impact of an improved longwave radiation model, rrtm, on the energy budget and thermodynamic properties of the NCAR Community Climate Model, CCM3. *J. Geophys. Res.* **105**, 14873–14890 (2000).
70. Fouquart, Y. Computations of solar heating of the earth's atmosphere: a new parameterization. *Beitraege Zur. Phys. Atmos.* **53**, 35 (1980).
71. Mascart, P. & Bougeault, P. The meso-nh atmospheric simulation system: Scientific documentation. *Part III: Physics. Météo-France Tech. Rep* (2011).
72. Lenderink, G. & Holtslag, A. A. An updated length-scale formulation for turbulent mixing in clear and cloudy boundary layers. *Q. J. R. Meteorol. Soc.* **130**, 3405–3427 (2004).
73. Masson, V. et al. The surfexv7. 2 land and ocean surface platform for coupled or offline simulation of earth surface variables and fluxes. *Geosci. Model Dev.* **6**, 929–960 (2013).
74. Boone, A. Description du schema de neige isba-es (explicit snow). *Note Cent. Météo Fr./CNRM* **70**, 53 (2002).
75. Brun, É et al. Le modèle de manteau neigeux crocus et ses applications. *La MétéOrol.* **2012**, 44–54 (2012).
76. Vionnet, V. et al. The detailed snowpack scheme crocus and its implementation in SURFEX v7. 2. *Geosci. Model Dev.* **5**, 773–791 (2012).
77. Morlighem, M. et al. Deep glacial troughs and stabilizing ridges unveiled beneath the margins of the Antarctic ice sheet. *Nat. Geosci.* **13**, 132–137 (2020).
78. Crosta, X. et al. Antarctic sea ice over the past 130 000 years—part 1: a review of what proxy records tell us. *Climate* **18**, 1729–1756 (2022).

Acknowledgements

R.M.'s participation in this research was supported by Ocean Cryosphere Exchanges in Antarctica: Impacts on Climate and the Earth system, OCEAN ICE, which is funded by the European Union, Horizon Europe Funding Programme for research and innovation under grant agreement No. 101060452, 10.3030/101060452. OCEAN ICE contribution number 34. J.A.T.-A. was supported by the ESA project Polar Ice Sheets in Climate

models and Earth Observation (PISCO) ESA Contract No. 4000148150/25/1-LR. We acknowledge the generous help and support of the ESA climate change initiative for the AIS and for Sea Ice, without whose climate data records this study would not have been possible. We also acknowledge the support of the European Centre for Medium Range Weather Forecasting for computational resources in special project spdkmott. Ideas in this manuscript were initially provoked during M.K.'s PhD visit to DMI and subsequently developed further during a research stay at the University of Canterbury, funded under the project number ALWPP.2019.003 of the research programme NPP, which is (partly) financed by the Dutch Research Council (NWO).

Author contributions

All authors contributed to the development of the ideas and methods presented in this study. J.A. Torres-Alvarez conducted the HCLIM43 simulations, and M. Kolbe performed the atmospheric river detection. M. Kolbe carried out the data analysis and wrote the main manuscript, with input from R. Mottram, J.A. Torres-Alvarez, R. Bintanja, E. van der Linden, and M. Katurji.

Competing interests

The authors declare no competing interests.

Additional information

Supplementary information The online version contains supplementary material available at <https://doi.org/10.1038/s43247-026-03242-3>.

Correspondence and requests for materials should be addressed to Marlen Kolbe.

Peer review information *Communications Earth & Environment* thanks Masashi Niwano, Jinfei Wang and the other anonymous reviewer(s) for their contribution to the peer review of this work. Primary handling editors: Shin Sugiyama and Nicola Colombo. A peer review file is available.

Reprints and permissions information is available at <http://www.nature.com/reprints>

Publisher's note Springer Nature remains neutral with regard to jurisdictional claims in published maps and institutional affiliations.

Open Access This article is licensed under a Creative Commons Attribution 4.0 International License, which permits use, sharing, adaptation, distribution and reproduction in any medium or format, as long as you give appropriate credit to the original author(s) and the source, provide a link to the Creative Commons licence, and indicate if changes were made. The images or other third party material in this article are included in the article's Creative Commons licence, unless indicated otherwise in a credit line to the material. If material is not included in the article's Creative Commons licence and your intended use is not permitted by statutory regulation or exceeds the permitted use, you will need to obtain permission directly from the copyright holder. To view a copy of this licence, visit <http://creativecommons.org/licenses/by/4.0/>.

© The Author(s) 2026